Electromagnetically-induced-transparency spectroscopy of high-lying Rydberg states in ^{39}K

Yuqi Zhu,[1,*] Sumita Ghosh,[1,2] S. B. Cahn,[1] M. J. Jewell,[1] D. H. Speller,[3] and Reina H. Maruyama[1,†]

[1]*Wright Laboratory, Department of Physics, Yale University, New Haven, Connecticut 06520, USA*

[2]*Department of Applied Physics, Yale University, New Haven, Connecticut 06520, USA*

[3]*Department of Physics, Johns Hopkins University, Baltimore, Maryland 21218, USA*

(Received 8 December 2021; accepted 28 March 2022; published 14 April 2022)

We present a study of the Rydberg spectrum in ^{39}K for nS and $nD_{3/2}$ series connected to $5\,^2P_{1/2}$ using two-photon spectroscopy based on electromagnetically induced transparency in a heated vapor cell. We observed some 80 transitions from $5P_{1/2}$ to Rydberg states with principal quantum numbers $n \sim 50$–90, and determined their transition frequencies and state energies with sub-GHz precision. Our spectroscopy results lay the groundwork for using Rydberg atoms as sensitive microwave photon detectors in searches for dark matter axions in the ∼40–200 μeV mass range, which is a prime range for future axion searches suggested by theory studies.

DOI: 10.1103/PhysRevA.105.042808

I. INTRODUCTION

The axion is a well-motivated solution to the strong charge-parity (CP) problem in quantum chromodynamics (QCD), and is also a natural dark matter candidate [1–4]. Depending on the cosmological history, a wide range of axion masses, $m_a \sim 10^{-6}$–10^3 μeV, can provide the correct abundance of dark matter [5]. Due to this wide range and the extremely weak coupling to matter required by benchmark QCD models [6,7], the axion remains undetected. Among the ongoing axion searches, the most sensitive searches are resonant microwave cavity experiments, covering the axion mass range $m_a \sim 0.2$–25 μeV [8–13]. They make use of the axion-to-photon conversion in a strong magnetic field and enhance the conversion by tuning the cavity's resonance to the hypothetical mass [14]. Given the typical parameters in an ongoing microwave cavity experiment [13], there are ∼0.3 photons per second, or equivalently $\sim 10^{-24}$ W at $m_a = 19$ μeV, converted from axions of the Milky Way halo [15]. Therefore, making sensitive and low-noise measurements of the photon number is critical for axion detection.

This study is motivated by the potential of using potassium atoms in Rydberg states as sensitive microwave probes in a resonant cavity search for dark matter axions [16,17]. Rydberg atoms are well suited to single-photon detection and microwave electrometry for having strong coupling to electromagnetic fields and long radiative lifetimes. In single-photon detection via absorption of the axion converted photon, the primary source of measurement background and noise is blackbody photons. At cryogenic temperatures, single-photon detectors are more compelling than linear amplifiers for searches at higher masses, $m_a > 40$ μeV (≈10 GHz) [18]. Previously ^{85}Rb Rydberg atoms have been considered for this application [16,19]. Compared to rubidium, dipole transitions between low-angular-momentum states in ^{39}K Rydberg atoms are less sensitive to the dc Stark effect for having similar polarizabilities. Therefore single-photon detection would be less sensitive to stray electric fields. To enhance the sensitivity to axion, a suitable detection scheme can be chosen by matching the resonant frequency of a dipole transition between Rydberg states to the target axion mass. For instance, to search at $m_a \approx 40$ μeV, the most sensitive Rydberg states—with dipole transitions in the vicinity—would have principal quantum numbers $n \sim 90$. According to some recent calculations, $m_a \sim 40$–200 μeV (≈10–50 GHz) is a highly probable mass range [20–22]. High-lying Rydberg states with $n \sim 60$–90 in ^{39}K would be particularly relevant to future axion searches in this mass range (see the Appendix for further details). However, only a few of the Rydberg states with $n > 50$ have been identified in previous spectroscopy studies [23–26]. Therefore, we study the energy spectrum of high-lying Rydberg states with $n \sim 50$–90 using an all-optical detection based on electromagnetically induced transparency (EIT) [27–29]. Broadly, beyond single-photon detection, Rydberg and Rydberg-dressed atoms have attracted interest as tools for quantum many-body physics and quantum information [30,31]. High-lying Rydberg states have a longer lifetime compared to low-lying states, as the lifetime scales as n^3 for the low-angular-momentum case.

In the remainder of this paper, we describe the experiment, including the Rydberg excitation scheme, experimental setup, and analysis procedure, in Sec. II. Then in Sec. III, we present the spectroscopy data with comparisons to other literature values, and then the derivation of quantum defects and ionization energies from data. In Sec. IV, we give a summary and outlook.

II. EXPERIMENT

In this experiment, the Rydberg excitation involves two resonant transitions connected to the $5\,^2P_{1/2}$ intermediate state: The first transition, $4S$-$5P_{1/2}$, is at about 405 nm, and

*yuqi.zhu@yale.edu
†reina.maruyama@yale.edu

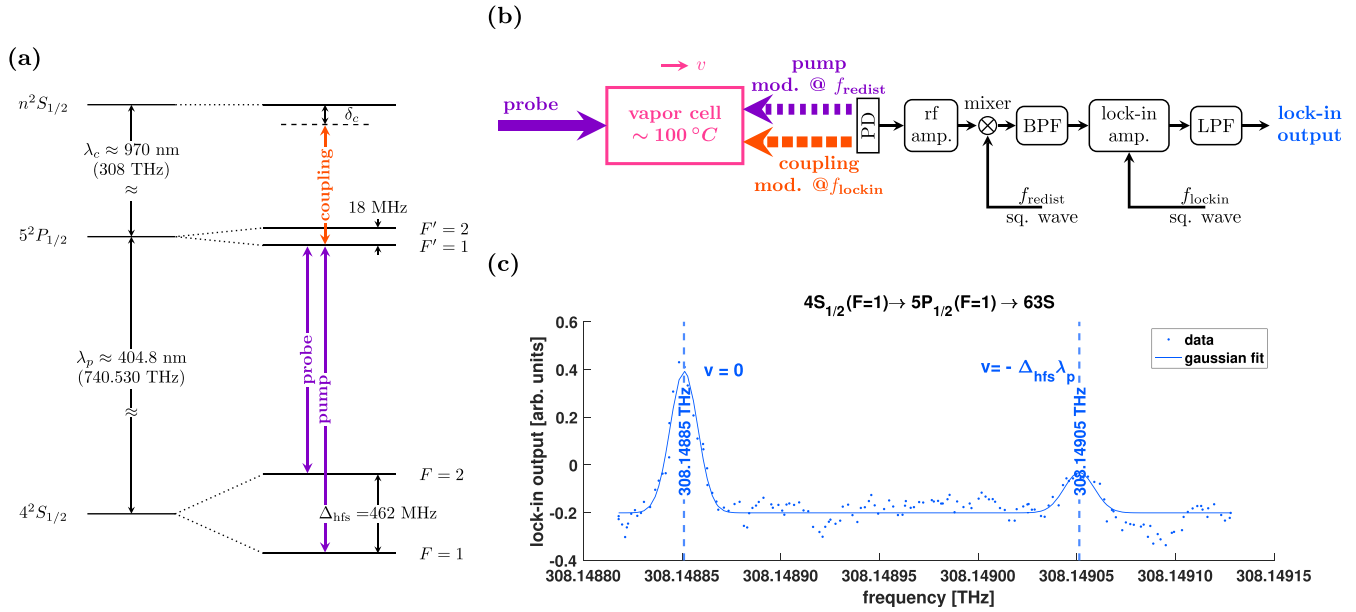

FIG. 1. (a) Energy levels and transitions in EIT. In EIT spectroscopy, the probe and pump frequencies are fixed while the frequency of the coupling beam is scanned to identify transitions from $5\,^2P_{1/2}$ to Rydberg states. When coupling frequency is on resonance, i.e., the coupling detuning $\delta_c = 0$, maximum probe transmission is attained. (b) Experimental setup. All three beams are aligned to overlap with each other in a vapor cell heated to $\sim$100 °C. The intensities of the coupling and pump beams are modulated at different frequencies for lock-in detection (f_{lockin}) and ground-state population redistribution (f_{redist}), respectively. The lock-in output is produced by doubly demodulating the amplified transmission signal. (c) An EIT spectrum near the $5P_{1/2}$-$63S$ Rydberg transition. Each data point is averaged over ten samples, and the peak locations, indicated by dashed lines, are found by fitting the spectrum to a sum of two Gaussian functions.

the second Rydberg transition, $5P_{1/2}$-$\{nS, nD_{3/2}\}$, at about 970 nm for $n \sim 50$–90. Alternatively, one can use one of the $4P$ states as the intermediate state for Rydberg excitation. The transitions between the intermediate state ($4P$ or $5P$) and Rydberg states are usually weak. For instance, the dipole matrix elements of transitions between $5P_{1/2}$ and Rydberg levels with $n \sim 50$–90 are on the order of $0.01ea_0$, which is about 100 times weaker than the D_2 line used in laser cooling and 10 times weaker than the $4S$-$5P_1/2$ transition. Therefore, the former scheme involving $5P$ presents a technological advantage—the small dipole matrix element of the transition between a Rydberg state and the intermediate $5P$ state can be matched by a powerful infrared laser. On a more fundamental level, however, the low-high wavelength ordering makes observing EIT challenging. Consider an atom moving at velocity v in the laboratory frame along the propagation direction of the probe beam that drives the $4S$-$5P_{1/2}$ transition. Because the probe wavelength ($\lambda_p = 2\pi/k_p \approx 405$ nm) is shorter than the coupling wavelength ($\lambda_c = 2\pi/k_c \approx 970$ nm), the one-photon Doppler shift $-k_p v$ has the same sign as the two-photon Doppler shift $-(k_p v - k_c v)$. Consequently, the transparency window as a function of the coupling detuning no longer exists, and the EIT feature in Doppler-averaged absorption is smaller by many orders of magnitude than that in a system where the probe wavelength is longer than the coupling wavelength [32,33].

To mitigate the suppression of EIT, we implement the velocity-selective EIT scheme presented in Ref. [29], which combines lock-in detection with an optical pumping scheme that eliminates any dark states in $4S$. Figure 1(a) shows the relevant energy levels and transitions. The pump and probe are tuned to be on resonance with $4S(F = 1)$-$5P_{1/2}(F' = 1)$ and $4S(F = 2)$-$5P_{1/2}(F' = 1)$, respectively. They come from the same external cavity diode laser [(ECDL) model TOPTICA DL PRO] and the frequency of the pump beam is offset by the ground-state hyperfine splitting Δ_{hfs} using a double-pass acousto-optic modulator setup. The frequency of the ECDL is locked using a Doppler-free saturated absorption signal as the reference. The resulting uncertainty is less than 9 MHz—half the hyperfine splitting of $5P_{1/2}$. The probe and pump deliver about 2 and 10 mW, respectively, to the experiment, and their diameters are roughly equal, $\sim$2 mm. The coupling beam provides 50–60 mW depending on the specific wavelength, and its diameter is $\sim$0.5 mm. Figure 1(b) shows the experimental setup. To look for the small EIT feature in the probe transmission measured by a photodiode (PD), the lock-in technique is applied—the lock-in modulation is added by chopping the coupling beam at $f_{\text{lockin}} \approx 1.3$ kHz. In addition to modulating the intensity of the coupling beam, the intensity of the pump beam is also modulated with 100% modulation intensity by a square wave in order to reduce the population imbalance between the two hyperfine ground states due to strong optical pumping on the 405-nm transition. The redistribution frequency $f_{\text{redist}} = 25$ kHz is chosen to be slower than the interatomic collision rate, which is about 50 kHz given the cell temperature and the 2-mm beam size [33]. This effectively modulates the population hole and peak near $v = 0$ at f_{redist}. The transmission signal is amplified by the PD and an additional radio-frequency (rf) amplifier (amp.) before being doubly demodulated by mixing first with a square wave of frequency f_{redist} at an rf mixer and then with a square wave of frequency f_{lockin} in a commercial lock-in amplifier (Stanford

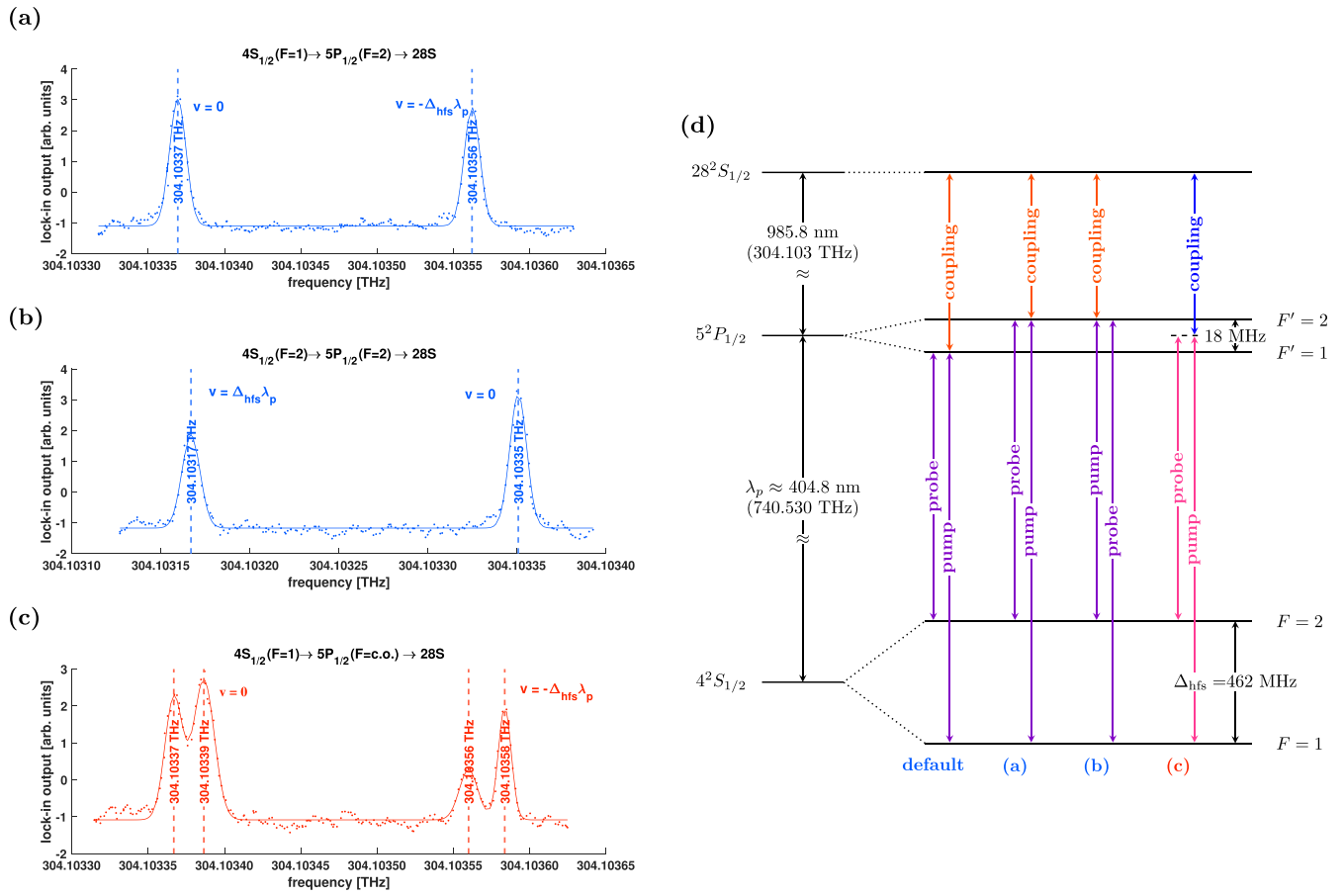

FIG. 2. Optical pumping in EIT. (a), (b) The pump beam drives a resonance transition between two hyperfine levels. (c) The pump beam drives a crossover transition on resonance. (d) EIT schemes used in (a)–(c).

Research 510) with built-in input and output filters. A band-pass filter (BPF) is applied to the input signal; it centers at f_{lockin} and has a 6-dB roll-off in either direction. A low-pass filter (LPF) is applied to the output after the demodulation; it has a cutoff frequency of 0.53 Hz and provides 6 dB/oct attenuation. The lock-in output is eventually used to determine the Rydberg transition frequencies.

Figure 1(c) shows an example of an EIT spectrum near the $5P_{1/2}$-$28S$ transition. The horizontal axis shows the frequency of the coupling beam measured by a wave meter (HighFinesse WS/7) whose absolute accuracy and resolution are 60 and 1 MHz, respectively. Because the pump and probe frequencies are offset by Δ_{hfs}, two velocity groups are observed in the EIT spectrum. For the EIT scheme in Fig. 1(a), they are $v = 0$ and $v = -\Delta_{\text{hfs}}\lambda_p$. By convention, v, the velocity in the laboratory frame, is positive if it is parallel to the arrow above the cell in Fig. 1(b). The $v = -\Delta_{\text{hfs}}\lambda_p$ atoms absorb blueshifted photons from the probe beam and redshifted photons from the coupling beam. Thus the maximum transmission, also the most efficient Rydberg excitation for this velocity group, occurs at a higher frequency than that for $v = 0$ atoms that absorb from the pump and coupling beams. We note that our spectrum consists of two peaks instead of four as in Ref. [29]. Comparing different optical pumping schemes in EIT (Fig. 2), we see that when the pump is on resonance with a transition between energy eigenstates, only one intermediate hyperfine level is populated. The locations of the $v = 0$ peaks are consistent in different spectra, and the separation between the $v = 0$ and $v = -\Delta_{\text{hfs}}\lambda_p$ peaks is $\Delta_{\text{hfs}}\frac{\lambda_p}{\lambda_c} \approx 190$ MHz in all cases.

III. RESULTS

All observed Rydberg levels, nS and $nD_{3/2}$, can be found in Table I, where f_c is the measured coupling frequency from $5P_{1/2}(F' = 1)$ to the Rydberg state and $E_{n,l,j}$ is the measured state energy relative to the $4S(F = 1)$ hyperfine ground state. Compared to other experimentally measured energies of ^{39}K Rydberg states (Table II), ours agree with the most recent results from Ref. [26] within uncertainties (except for $68S$) but differ from earlier results in Refs. [23,25]. The observed transition frequency of the first transition, $4S$-$5P_{1/2}$, is not consistent with the NIST value by 570(60) MHz [23,34] but consistent with the reported value in Ref. [29].

From measured state energies, the ionization energy E_∞ and the quantum defect $\delta(n, l, j)$ can be determined by fitting to [35]

$$E_{n,l,j} = E_\infty - \frac{\text{Ry}^*}{[n - \delta(n, l, j)]^2}, \tag{1}$$

where $\text{Ry}^* = 109\,735.770\,665\,6$ cm^{-1} is the Rydberg constant for ^{39}K, numerically calculated from fundamental constants [36–38]. The quantum defect in (1) has a

TABLE I. Observed coupling frequencies (f_c) and energies ($E_{n,l,j}$) of Rydberg states. State energies are calculated by adding the measured transition energy of $4S(F=1)$-$5P_{1/2}(F=1)$, 24 701.399(2) cm^{-1}, to the coupling frequencies. The uncertainties (not shown) are systematic, 60 MHz for f_c and 0.003 cm^{-1} for $E_{n,l,j}$.

Ry. state	f_c [THz]	$E_{n,l,j}$ [cm^{-1}]
28S	304.10338	34845.196
50S	307.59958	34961.817
51S	307.65791	34963.762
52S	307.71275	34965.592
53S	307.76442	34967.315
54S	307.81309	34968.939
55S	307.85901	34970.470
56S	307.90247	34971.920
57S	307.94354	34973.290
58S	307.98240	34974.586
59S	308.01923	34975.815
61S	308.08734	34978.087
62S	308.11887	34979.139
63S	308.14885	34980.139
64S	308.17741	34981.091
65S	308.20458	34981.998
66S	308.23049	34982.862
67S	308.25526	34983.688
68S	308.27882	34984.474
69S	308.30141	34985.227
70S	308.32297	34985.947
71S	308.34360	34986.635
72S	308.36339	34987.295
73S	308.38225	34987.924
74S	308.40046	34988.531
75S	308.41784	34989.111
76S	308.43454	34989.668
77S	308.45052	34990.201
78S	308.46596	34990.716
79S	308.48077	34991.210
80S	308.49500	34991.685
81S	308.50868	34992.141
82S	308.52186	34992.581
83S	308.53457	34993.005
84S	308.54681	34993.413
85S	308.55861	34993.807
86S	308.56998	34994.186
87S	308.58091	34994.550
88S	308.59153	34994.905
89S	308.60176	34995.246
48$D_{3/2}$	307.59373	34961.622
49$D_{3/2}$	307.65242	34963.579
50$D_{3/2}$	307.70760	34965.420
51$D_{3/2}$	307.75958	34967.154
52$D_{3/2}$	307.80852	34968.786
53$D_{3/2}$	307.85471	34970.327
54$D_{3/2}$	307.89837	34971.784
55$D_{3/2}$	307.93967	34973.161
56$D_{3/2}$	307.97873	34974.464
57$D_{3/2}$	308.01576	34975.699
58$D_{3/2}$	308.05089	34976.871
59$D_{3/2}$	308.08421	34977.982
60$D_{3/2}$	308.11589	34979.039
61$D_{3/2}$	308.14598	34980.043
62$D_{3/2}$	308.17471	34981.001
63$D_{3/2}$	308.20202	34981.912
64$D_{3/2}$	308.22805	34982.780
65$D_{3/2}$	308.25291	34983.609
66$D_{3/2}$	308.27661	34984.400
67$D_{3/2}$	308.29927	34985.156
68$D_{3/2}$	308.32094	34985.879
69$D_{3/2}$	308.34165	34986.570
70$D_{3/2}$	308.36152	34987.233
71$D_{3/2}$	308.38045	34987.864
72$D_{3/2}$	308.39873	34988.474
73$D_{3/2}$	308.41619	34989.056
74$D_{3/2}$	308.43294	34989.615
75$D_{3/2}$	308.44901	34990.151
76$D_{3/2}$	308.46451	34990.668
77$D_{3/2}$	308.47937	34991.163
78$D_{3/2}$	308.49364	34991.639
79$D_{3/2}$	308.50737	34992.097
80$D_{3/2}$	308.52061	34992.539
81$D_{3/2}$	308.53334	34992.964
82$D_{3/2}$	308.54564	34993.374
83$D_{3/2}$	308.55748	34993.769
84$D_{3/2}$	308.56888	34994.149
85$D_{3/2}$	308.57987	34994.516
86$D_{3/2}$	308.59050	34994.870
87$D_{3/2}$	308.60079	34995.214

phenomenological expression,

$$\delta(n, l, j) = \delta_0 + \frac{\delta_2}{(n-\delta_0)^2} + o(n^4), \tag{2}$$

where $\{\delta_{2i}\}_{i=0}$ are the Rydberg-Ritz coefficients specific to an angular momentum configuration [35,39]. The quantum defect most strongly depends on l, the orbital angular momentum, as it is caused by the penetration of the electron orbital into the ionic core. Writing it as a series expansion is in the same spirit of adding spherically symmetric corrections to the Coulomb potential in perturbation theory [40]. Figure 3 shows a plot of fit results for both term series. The ionization energy is 35 009.805(3) cm^{-1} for both series. The quantum defects, to leading order and independent of n, are $\delta_0 = 2.181(1)$ for the nS states and $\delta_0 = 0.277(1)$ for $nD_{3/2}$. Statistical uncertainties from fitting are negligible, and the quoted uncertainties are systematically propagated from the wave meter's accuracy. Our data of high-lying Rydberg states are not very sensitive to high-order terms in (1). Notwithstanding this, our δ_0 agrees with results derived using similar methods in Refs. [23–26,34,38]. Our ionization energy is consistent with the reported value in Ref. [26], but it appears to be lower than most other reported values [23–25,34,38].

IV. SUMMARY AND OUTLOOK

In summary, we directly measured the transition frequencies between $5P_{1/2}$ and 81 Rydberg states with $n \sim 50$–90 using two-photon spectroscopy based on velocity-selective EIT, and calculated the their state energies. Out of the 81

TABLE II. Comparing observed state energies relative to the $4S(F = 1)$ ground state to other experimental results. The uncertainty in our values is systematic, due to the wave meter, 80 MHz ≈ 0.003 cm^{-1}.

	State energy $E_{n,l,j}$ [cm^{-1}]			
Excited state	Observed	NIST [34,41]	Ref. [25]	Ref. [26]
$5P_{1/2}$	24701.399(2)	24701.38(3)		
$28S$	34845.196(3)	34845.2158(7)	34845.214(3)	34845.18(3)
$50S$	34961.817(3)		34961.835(3)	34961.80(3)
$54S$	34968.939(3)			34968.94(3)
$55S$	34970.470(3)		34970.493(3)	
$56S$	34971.920(3)			34971.89(3)
$62S$	34979.139(3)			34979.13(3)
$66S$	34982.862(3)			34982.83(3)
$68S$	34984.474(3)			34984.36(3)
$70S$	34985.947(3)			34985.93(3)

Rydberg states we found, 9 have been previously identified in experiments; the state energies determined using our method are in agreement with most recent experimental results.

As searches for the QCD axion extend to higher masses, specifically for $m_a > 40$ μeV, single-photon detection will become increasingly relevant. This work marks a step towards developing single-photon detection using Rydberg atoms for this application. Being able to populate high-n low-angular-momentum Rydberg states via two-photon transitions is fundamental to preparing atoms into other detection states, such as circular Rydberg states, which are Rydberg states with the maximum possible orbital angular momentum l projection along the quantization axis ($l = n - 1 = |m_l|$). The Doppler-free EIT spectrum will also enable us to stabilize the frequency of the 970-nm laser driving the Rydberg transition to good precision and accuracy. Furthermore, the spectroscopy data may also be relevant to future applications of Rydberg and Rydberg-dressed atoms for quantum many-body physics and quantum information.

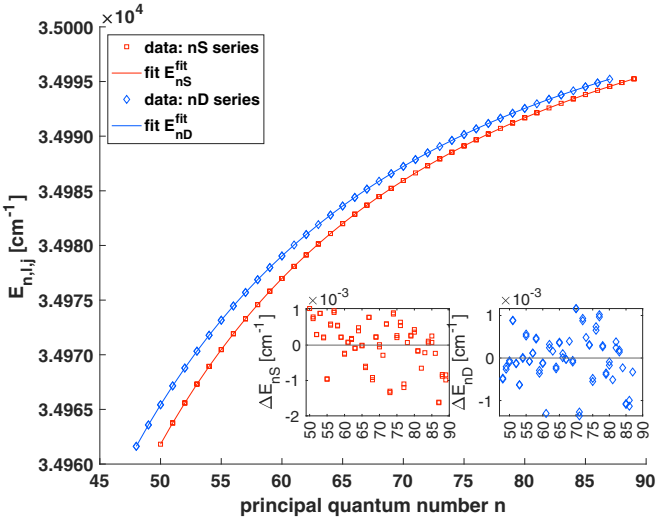

FIG. 3. State energies fitted to the Rydberg energy equation with two Rydberg-Ritz coefficients. Insets show the difference between data and fit for each series $\Delta E = E - E^{\text{fit}}$. The adjust residual squared (R^2) deviates from 1 by 10^{-14} and 10^{-9} for nS and $nD_{3/2}$ series, respectively.

ACKNOWLEDGMENTS

We would like to thank Mark Saffman and Michael Peper for fruitful discussions. We would also like to thank Gabe Hoshino, Elizabeth Ruddy, Annie Giman, and Sophia Getz for support on the experiment. Y.Z., S.G., S.C., M.J., and R.M. are supported in part by the Department of Energy under Grant No. DE-AC02-07CH11359; S.G. is supported in part by the National Science Foundation under Grant No. DMR-1747426. D.S. would like to thank Johns Hopkins University.

APPENDIX: RYDBERG ATOM-BASED MICROWAVE DETECTION

In this Appendix, we discuss the prospect of microwave detection using Rydberg atoms in the context of an axion search to clarify why Rydberg states with $n \sim 60$–90 are particularly relevant to axion searches in the $m_a \sim 40$–200 μeV range. Suppose, as in CARRACK II, the detection mechanism is a combination of microwave absorption and selective field ionization [17]. Since the frequency of the axion-converted photon we wish to detect is equal to m_a, a suitable transition for a given axion mass target should be as close to the axion mass as possible to increase the probability of absorption.

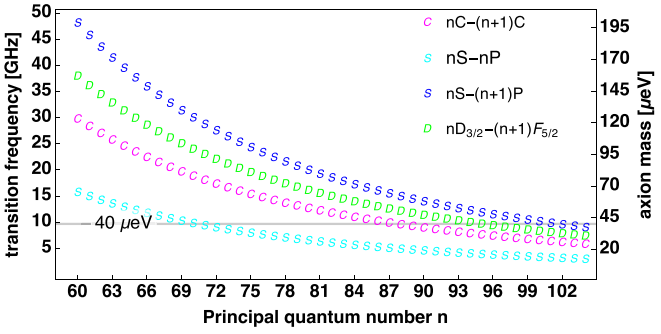

FIG. 4. Transition frequency vs principal quantum number. The y axes are equivalent and only different in units. The most sensitive Rydberg states for $m_a = 40$ μeV ≈ 10 GHz are $70S$ (or $101S$), $87C$, and $95D_{3/2}$. The fine-structure splitting within nP is on the order of 0.5 μeV. However, the resulting difference in transition frequency is not resolved in this plot.

There are potentially many suitable transitions connecting different initial and final states. Their transition frequencies can be calculated using the alkali Rydberg calculator (ARC) [42]; using the default parameters in ARC, quantum defects and ionization energy used to determine state energies are based on Ref. [24]. Figure 4 shows the transition frequency versus principal quantum number for dipole transitions starting from three types of initial states. nS and $nD_{3/2}$ are readily accessible via the two-photon excitation scheme used in this work. nC are representative of high-l states, which have much longer lifetimes and larger transition dipole moments compared to low-l states. Preparing them requires an additional transferring step, known as the adiabatic rapid passage (ARP) [43], after the two-photon optical excitation.

[1] R. D. Peccei and H. R. Quinn, *CP* Conservation in the Presence of Pseudoparticles, Phys. Rev. Lett. **38**, 1440 (1977).

[2] R. D. Peccei and H. R. Quinn, Constraints imposed by *CP* conservation in the presence of pseudoparticles, Phys. Rev. D **16**, 1791 (1977).

[3] S. Weinberg, A New Light Boson? Phys. Rev. Lett. **40**, 223 (1978).

[4] F. Wilczek, Problem of Strong P and T Invariance in the Presence of Instantons, Phys. Rev. Lett. **40**, 279 (1978).

[5] D. J. Marsh, Axion cosmology, Phys. Rep. **643**, 1 (2016).

[6] J. E. Kim, Weak-Interaction Singlet and Strong *CP* Invariance, Phys. Rev. Lett. **43**, 103 (1979).

[7] M. Dine, W. Fischler, and M. Srednicki, A simple solution to the strong *CP* problem with a harmless axion, Phys. Lett. B **104**, 199 (1981).

[8] N. Du, N. Force, R. Khatiwada, E. Lentz, R. Ottens, L. J. Rosenberg, G. Rybka, G. Carosi, N. Woollett, D. Bowring *et al.* (ADMX Collaboration), Search for Invisible Axion Dark Matter with the Axion Dark Matter Experiment, Phys. Rev. Lett. **120**, 151301 (2018).

[9] T. Braine, R. Cervantes, N. Crisosto, N. Du, S. Kimes, L. J. Rosenberg, G. Rybka, J. Yang, D. Bowring, A. S. Chou *et al.* (ADMX Collaboration), Extended Search for the Invisible Axion with the Axion Dark Matter Experiment, Phys. Rev. Lett. **124**, 101303 (2020).

[10] C. Bartram, T. Braine, E. Burns, R. Cervantes, N. Crisosto, N. Du, H. Korandla, G. Leum, P. Mohapatra, T. Nitta *et al.* (ADMX Collaboration), Search for "Invisible" Axion Dark Matter in the 3.3–4.2 μeV Mass Range, Phys. Rev. Lett. **127**, 261803 (2021).

[11] B. Brubaker, L. Zhong, Y. V. Gurevich, S. B. Cahn, S. K. Lamoreaux, M. Simanovskaia, J. R. Root, S. M. Lewis, S. Al Kenany, K. M. Backes *et al.*, First Results from a Microwave Cavity Axion Search at 24 μeV, Phys. Rev. Lett. **118**, 061302 (2017).

[12] L. Zhong, S. Al Kenany, K. M. Backes, B. M. Brubaker, S. B. Cahn, G. Carosi, Y. V. Gurevich, W. F. Kindel, S. K. Lamoreaux, K. W. Lehnert *et al.*, Results from phase 1 of the HAYSTAC microwave cavity axion experiment, Phys. Rev. D **97**, 092001 (2018).

[13] K. M. Backes, D. A. Palken, S. A. Kenany, B. M. Brubaker, S. B. Cahn, A. Droster, G. C. Hilton, S. Ghosh, H. Jackson, S. K. Lamoreaux *et al.*, A quantum enhanced search for dark matter axions, Nature (London) **590**, 238242 (2021).

[14] P. Sikivie, Experimental Tests of the "Invisible" Axion, Phys. Rev. Lett. **51**, 1415 (1983).

[15] P. Sikivie, Detection rates for "invisible"-axion searches, Phys. Rev. D **32**, 2988 (1985).

[16] M. Tada, Y. Kishimoto, K. Kominato, M. Shibata, H. Funahashi, K. Yamamoto, A. Masaike, and S. Matsuki, CARRACK II—a new large-scale experiment to search for axions with Rydberg-atom cavity detector, Nucl. Phys. B, Proc. Suppl. **72**, 164 (1999).

[17] K. Yamamoto, M. Tada, Y. Kishimoto, M. Shibata, K. Kominato, T. Ooishi, S. Yamada, T. Saida, H. Funahashi, A. Masaike, and S. Matsuki, The Rydberg-atom-cavity axion search, in *Dark Matter in Astro- and Particle Physics*, edited by H. V. Klapdor-Kleingrothaus (Springer, Berlin, 2001), pp. 638–645.

[18] S. K. Lamoreaux, K. A. van Bibber, K. W. Lehnert, and G. Carosi, Analysis of single-photon and linear amplifier detectors for microwave cavity dark matter axion searches, Phys. Rev. D **88**, 035020 (2013).

[19] M. Tada, Y. Kishimoto, K. Kominato, M. Shibata, S. Yamada, T. Haseyama, I. Ogawa, H. Funahashi, K. Yamamoto, and S. Matsuki, Single-photon detection of microwave blackbody radiations in a low-temperature resonant-cavity with high Rydberg atoms, Phys. Lett. A **349**, 488 (2006).

[20] G. Ballesteros, J. Redondo, A. Ringwald, and C. Tamarit, Unifying Inflation with the Axion, Dark Matter, Baryogenesis, and the Seesaw Mechanism, Phys. Rev. Lett. **118**, 071802 (2017).

[21] M. Gorghetto, E. Hardy, and G. Villadoro, More Axions from Strings, SciPost Phys. **10**, 50 (2021).

[22] M. Buschmann, J. W. Foster, A. Hook, A. Peterson, D. E. Willcox, W. Zhang, and B. R. Safdi, Dark matter from axion strings with adaptive mesh refinement, Nat. Commun. **13**, 1049 (2022).

[23] C.-J. Lorenzen, K. Niemax, and L. Pendrill, Precise measurements of ^{39}K nS and nD energy levels with an evaluated wavemeter, Opt. Commun. **39**, 370 (1981).

[24] C.-J. Lorenzen and K. Niemax, Quantum defects of the $n^2P_{1/2,3/2}$ levels in ^{39}KI and ^{85}RbI, Phys. Scr. **27**, 300 (1983).

[25] D. C. Thompson, M. S. O'Sullivan, B. P. Stoicheff, and G.-X. Xu, Doppler-free two-photon absorption spectrum of potassium, Can. J. Phys. **61**, 949 (1983).

[26] T.-L. Chen, S.-Y. Chang, Y.-J. Huang, K. Shukla, Y.-C. Huang, T.-H. Suen, T.-Y. Kuan, J.-T. Shy, and Y.-W. Liu, Inverted-ladder-type optical excitation of potassium Rydberg states with hot and cold ensembles, Phys. Rev. A **101**, 052507 (2020).

[27] K.-J. Boller, A. Imamoğlu, and S. E. Harris, Observation of Electromagnetically Induced Transparency, Phys. Rev. Lett. **66**, 2593 (1991).

[28] A. K. Mohapatra, T. R. Jackson, and C. S. Adams, Coherent Optical Detection of Highly Excited Rydberg States Using Electromagnetically Induced Transparency, Phys. Rev. Lett. **98**, 113003 (2007).

[29] W. Xu and B. DeMarco, Velocity-selective electromagnetically-induced-transparency measurements of potassium Rydberg states, Phys. Rev. A **93**, 011801(R) (2016).

[30] M. Saffman, T. G. Walker, and K. Mølmer, Quantum information with Rydberg atoms, Rev. Mod. Phys. **82**, 2313 (2010).

[31] G. Pupillo, A. Micheli, M. Boninsegni, I. Lesanovsky, and P. Zoller, Strongly Correlated Gases of Rydberg-Dressed Atoms: Quantum and Classical Dynamics, Phys. Rev. Lett. **104**, 223002 (2010).

[32] J. R. Boon, E. Zekou, D. McGloin, and M. H. Dunn, Comparison of wavelength dependence in cascade-, Λ-, and Vee-type schemes for electromagnetically induced transparency, Phys. Rev. A **59**, 4675 (1999).

[33] A. Urvoy, C. Carr, R. Ritter, C. S. Adams, K. J. Weatherill, and R. Lw, Optical coherences and wavelength mismatch in ladder systems, J. Phys. B: At., Mol. Opt. Phys. **46**, 245001 (2013).

[34] J. E. Sansonetti, Wavelengths, transition probabilities, and energy levels for the spectra of potassium (KI through KXIX), J. Phys. Chem. Ref. Data **37**, 7 (2008).

[35] T. F. Gallagher, *Rydberg Atoms*, Cambridge Monographs on Atomic, Molecular and Chemical Physics (Cambridge University Press, Cambridge, UK, 1994).

[36] P. J. Mohr, D. B. Newell, and B. N. Taylor, CODATA recommended values of the fundamental physical constants: 2014, Rev. Mod. Phys. **88**, 035009 (2016).

[37] J. Coursey, D. Schwab, J. Tsai, and R. Dragoset, *Atomic Weights and Isotopic Compositions (version 4.1)* (National Institute of Standards and Technology, Gaithersburg, MD, 2015), http://physics.nist.gov/Comp (accessed 11 January 2022).

[38] M. Peper, F. Helmrich, J. Butscher, J. A. Agner, H. Schmutz, F. Merkt, and J. Deiglmayr, Precision measurement of the ionization energy and quantum defects of ^{39}K I, Phys. Rev. A **100**, 012501 (2019).

[39] W. C. Martin, Series formulas for the spectrum of atomic sodium (Na I), J. Opt. Soc. Am. **70**, 784 (1980).

[40] G. W. F. Drake and R. A. Swainson, Quantum defects and the $1/n$ dependence of Rydberg energies: Second-order polarization effects, Phys. Rev. A **44**, 5448 (1991).

[41] A. Kramida, Yu. Ralchenko, J. Reader, and NIST ASD Team, *NIST Atomic Spectra Database (ver. 5.8)*, (National Institute of Standards and Technology, Gaithersburg, MD, 2020), https://physics.nist.gov/asd (accessed 23 August 2021).

[42] N. Sibalic, J. Pritchard, C. Adams, and K. Weatherill, ARC: An open-source library for calculating properties of alkali Rydberg atoms, Comput. Phys. Commun. **220**, 319 (2017).

[43] A. Signoles, E. K. Dietsche, A. Facon, D. Grosso, S. Haroche, J. M. Raimond, M. Brune, and S. Gleyzes, Coherent Transfer Between Low-Angular-Momentum and Circular Rydberg States, Phys. Rev. Lett. **118**, 253603 (2017).